

PAPER • OPEN ACCESS

Porous polymeric microparticles foamed with supercritical CO₂ as scattering white pigments

To cite this article: Luisa Maren Borgmann *et al* 2023 *Bioinspir. Biomim.* **18** 026011

View the [article online](#) for updates and enhancements.

You may also like

- [Search for Gravitational Waves Associated with Gamma-Ray Bursts Detected by Fermi and Swift during the LIGO–Virgo Run O3b](#)
R. Abbott, T. D. Abbott, F. Acernese et al.
- [Searches for Gravitational Waves from Known Pulsars at Two Harmonics in the Second and Third LIGO–Virgo Observing Runs](#)
R. Abbott, H. Abe, F. Acernese et al.
- [A Search for Extragalactic Fast Blue Optical Transients in ZTF and the Rate of AT2018cow-like Transients](#)
Anna Y. Q. Ho, Daniel A. Perley, Avishay Gal-Yam et al.

Bioinspiration & Biomimetics



PAPER

Porous polymeric microparticles foamed with supercritical CO₂ as scattering white pigments

OPEN ACCESS

RECEIVED

13 October 2022

REVISED

10 January 2023

ACCEPTED FOR PUBLICATION

1 February 2023



PUBLISHED

23 February 2023

Original Content from this work may be used under the terms of the [Creative Commons Attribution 4.0 licence](#).

Any further distribution of this work must maintain attribution to the author(s) and the title of the work, journal citation and DOI.



Luisa Maren Borgmann¹ , Siegbert Johnsen², Cristine Santos de Oliveira³, Juliana Martins de Souza e Silva^{3,4}, Juan Li⁵ , Christoph Kirchlechner⁵, Guillaume Gomard^{1,6}, Gabriele Wiegand² and Hendrik Hölscher^{1,*}

¹ Institute of Microstructure Technology (IMT), Karlsruhe Institute of Technology (KIT), PO Box 3640, 76021 Karlsruhe, Germany

² Institute of Catalysis Research and Technology (IKFT), Karlsruhe Institute of Technology (KIT), PO Box 3640, 76021 Karlsruhe, Germany

³ Martin-Luther-Universität Halle-Wittenberg, Institute of Physics, 06120 Halle (Saale), Germany

⁴ Fraunhofer Institute for Microstructure of Materials and Systems IMWS, 06120 Halle (Saale), Germany

⁵ Institute for Applied Materials (IAM), Karlsruhe Institute of Technology (KIT), PO Box 3640, 76021 Karlsruhe, Germany

⁶ Carl Zeiss AG, Zeiss Innovation Hub, Hermann-von-Helmholtz-Platz 6, 76344 Eggenstein-Leopoldshafen, Germany

* Author to whom any correspondence should be addressed.

E-mail: hendrik.hoelscher@kit.edu

Keywords: supercritical CO₂ foaming, nano-pores, structural color, white pigments

Supplementary material for this article is available [online](#)

Abstract

Nowadays, titanium dioxide (TiO₂) is the most commercially relevant white pigment. Nonetheless, it is widely criticized due to its energy-intensive extraction and costly disposal of harmful by-products. Furthermore, recent studies discuss its potential harm for the environment and the human health. Environment-friendly strategies for the replacement of TiO₂ as a white pigment can be inspired from nature. Here whiteness often originates from broadband light scattering air cavities embedded in materials with refractive indices much lower than that of TiO₂. Such natural prototypes can be mimicked by introducing air-filled nano-scale cavities into commonly used polymers. Here, we demonstrate the foaming of initially transparent poly(methyl methacrylate) (PMMA) microspheres with non-toxic, inert, supercritical CO₂. The properties of the foamed, white polymeric pigments with light scattering nano-pores are evaluated as possible replacement for TiO₂ pigments. For that, the inner foam structure of the particles was imaged by phase-contrast x-ray nano-computed tomography (nano-CT), the optical properties were evaluated via spectroscopic measurements, and the mechanical stability was examined by micro compression experiments. Adding a diffusion barrier surrounding the PMMA particles during foaming allows to extend the foaming process towards smaller particles. Finally, we present a basic white paint prototype as exemplary application.

1. Introduction

Titanium dioxide (TiO₂) is the standard pigment when a perfect white color impression is needed because all wavelengths of visible light are scattered efficiently with nearly equal intensity [1]. Its production accounts for more than 90% of the global titanium mineral consumption [1]. The widespread use of TiO₂ as white pigment is mainly based on its high refractive index n , reaching 2.55–2.75 at a wavelength of 550 nm. Therefore, a high refractive index contrast between the embedding medium

(polymer, binder, etc) and the TiO₂ particles is achieved [1]. For the industrial production of TiO₂ pigments, naturally occurring titanium ores are refined by energy intensive procedures including the sulfate or the chloride process [1–3]. Many of the used chemicals, intermediates, and waste products are toxic, corrosive, or generally harmful to the environment [1, 3]. Moreover, rising costs for proper waste disposal increased the manufacturing costs [2] and triggered the search for the replacement of TiO₂ [4]. In addition, concerns grew that TiO₂ could be harmful to humans, especially for particle sizes in the

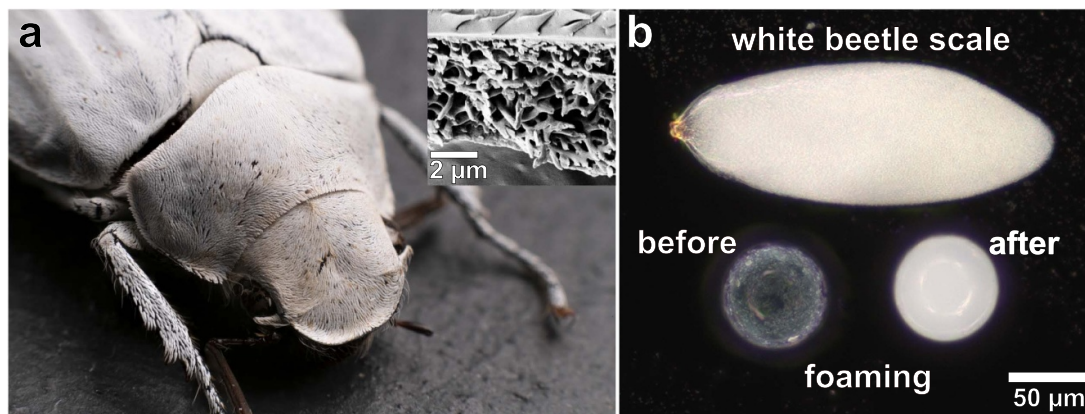


Figure 1. (a) The white beetle *Cyphochilus insulanus* is covered with white scales, which are only about 5–7 μm thick. They appear perfectly white to the naked eye because their porous structure results in broadband light scattering (see inset). This inner structure scatters light of all wavelengths perfectly. Reproduced with permission from Karlsruhe Institute of Technology. Image taken by Markus Breig. (b) Inspired by this effect PMMA particles serving as transparent matrix material can be equipped with air inclusions by foaming with supercritical CO_2 . Due to the light scattering caused by the pores the foamed particles become nearly as white as the beetle scales.

nanometer range [5–14]. Based on the safety assessment of the European Food Safety Authority (EFSA) from 2021 [15] the European Commission banned TiO_2 as a food additive in Europe in 2022 [16]. Due to this recent ban and the accumulating studies on potential health issues, it can be expected that the controversial debate on the use of TiO_2 will further intensify and reinforce the interest in alternative white pigments.

A look into nature shows that efficient light scattering can be achieved by air-filled cavities in a transparent matrix. Here the low refractive index of air compared to the surrounding medium provides the necessary refractive index contrast. Various species of plants, insects, and birds utilize cellulose [17], chitin [18], or keratin [19], respectively, and combine it with air voids to create bright white color impressions. A prominent example are the scales of the white beetle of the genus *Cyphochilus* shown in figure 1. They display a high reflectance over the visible range of about 60 to above 70% [18, 20] with very thin scales of only about 5–7 μm thickness [21, 22]. The porous network within these scales (see inset in figure 1(a)) generates maximum reflection for a minimum of material use [23]. The scales are composed of chitin, which exhibits a refractive index of only 1.55 at a wavelength of 550 nm [24]. This value is within the range of several industrially commonly used polymers. Thus these synthetic materials can effectively scatter light, when imbued with air inclusions. Indeed, there are polymer-based implementations making use of air voids, serving as extender particles for the partial substitution of TiO_2 . Hereby, a distinction can be made between particles that exclusively contain air inclusions [25, 26] and those that additionally contain TiO_2 particles [27, 28]. Typical TiO_2 -free hollow spheres possess particle sizes of about 400 nm with

a single air void enclosed in a few nanometers thin polymeric shell. These shells withstand mechanical loads during paint application and drying [29]. However, high mechanical strain could cause the destruction of the thin shell and result in loss in opacity [4]. Another strategy reported for aqueous latex paints can be to emulsify tiny droplets of a volatile fluid, which leaves cavities within the film by evaporation [27]. However, this can be considered a rather specific strategy for this particular paint type. Other strategies to replace TiO_2 include direct replacement with other materials such as e.g. ZnO or CaCO_3 , whereby the production of these is in turn associated with energy-intensive processes and by-products and are discussed more in detail, e.g. from Ruzsala *et al* [4].

Here we present the fabrication of porous polymer particles featuring multiple nano-sized air inclusions, instead of a single air void within a thin shell. The porous structure is introduced into initially transparent, monodisperse, robust, and commercially available poly(methyl methacrylate) (PMMA) microspheres. Environmentally friendly supercritical CO_2 foaming is utilized, which is suitable for a variety of polymers and has the advantage to leave no traces of solvents in the polymer [30]. With well-controllable process parameters, pore size and density and thereby light scattering properties of the particles are tailored. An additional advantage of the present approach is the formation of a protective, closed outer shell of a few micrometers around each porous core. The inner structure of the foamed particles and their resulting optical properties are investigated to identify the most suitable process parameters. The mechanical stability is examined by means of micro compression experiments. Finally, the suitability of the foamed particles for paints is demonstrated.

2. Materials and methods

2.1. Supercritical CO₂ foaming

The foaming process is based on the ability of CO₂ to act as a plasticizer for polymers with good CO₂ solubility [31]. This effect is noticeable through the considerable decrease in the glass transition temperature T_{glass} of the respective polymer [32, 33]. The pore formation process in polymers during foaming with supercritical CO₂ is sketched in figure 2(a). It consists of the following steps [34–36]: (a) The polymer is saturated with supercritical CO₂ under constant temperature and pressure conditions until the solubility limit is reached, whereby T_{glass} of the polymer decreases. (b) As the pressure is released, the solubility of CO₂ in the polymer decreases. It is supersaturated under the new conditions and nucleation occurs. (c) Pores start to grow due to CO₂ diffusing from the polymer matrix into nuclei of a critical size, whereby the T_{glass} increases again. (d) The foam structure finally stabilizes as T_{glass} reaches T_{sample} . Key parameters to control the pore density and size, are pressure, temperature and pressure drop rate. An unfoamed layer is created by CO₂ diffusion out of the polymer surface and should be kept as thin as possible here. The layer thickness decreases with increasing saturation pressure [37], therefore the highest applicable pressure of 50 MPa of our setup is used. Generally, the pore size increases with rising temperature [38], here foaming temperatures of 60 °C–150 °C were tested. Based on literature values for the diffusion coefficient of CO₂ in PMMA [39] and the spherical geometry of the particles [40], a saturation time of 30 min was determined to be sufficient for complete saturation of the 60 μm diameter particles.

2.1.1. Materials

As base material monodisperse, cross-linked PMMA microspheres (*Spheromers*[®] from Microbeads AS [41]) with diameters of 10, 20, 40 and 60 μm were used. These are frequently utilized as a mechanically robust additive for thermoplastics, coatings, and paints. PMMA has a great affinity for CO₂ and is well suited for supercritical CO₂ foaming [42]. Cross-linking modifies several properties, for instance the T_{glass} increases compared to conventional PMMA [43, 44]. Therefore a higher temperature range for successful foaming is expected compared to previous studies [45]. In a variation of the foaming process (see figure 2(b)), the microspheres were embedded in a diffusion barrier. This prevents the fast escape of CO₂ during the pressure release step as suggested by Orsi *et al* [40]. The barrier is made of water-soluble polyvinyl alcohol (PVA) with a molecular weight M_w of 200 K (*Merck KGaA*). In accordance with the suggested procedure, we used an aqueous 5% (wt vol⁻¹) PVA solution as embedding solution. The particles

were weighed into the solution in a concentration of either 1 wt% or 10 wt%. The first one was used for the preliminary examination by optical microscopy, the latter for the final procedure. The particle-containing solution was then filled into PDMS molds. After air-drying at room temperature for at least 72 h, a stable foil of PVA with enclosed PMMA particles was obtained. Since the CO₂ has to additionally diffuse through the enclosing PVA barrier, the saturation time was increased to 120 min. After foaming the barrier film was dissolved in H₂O, the particles were filtered out and air-dried for further examination.

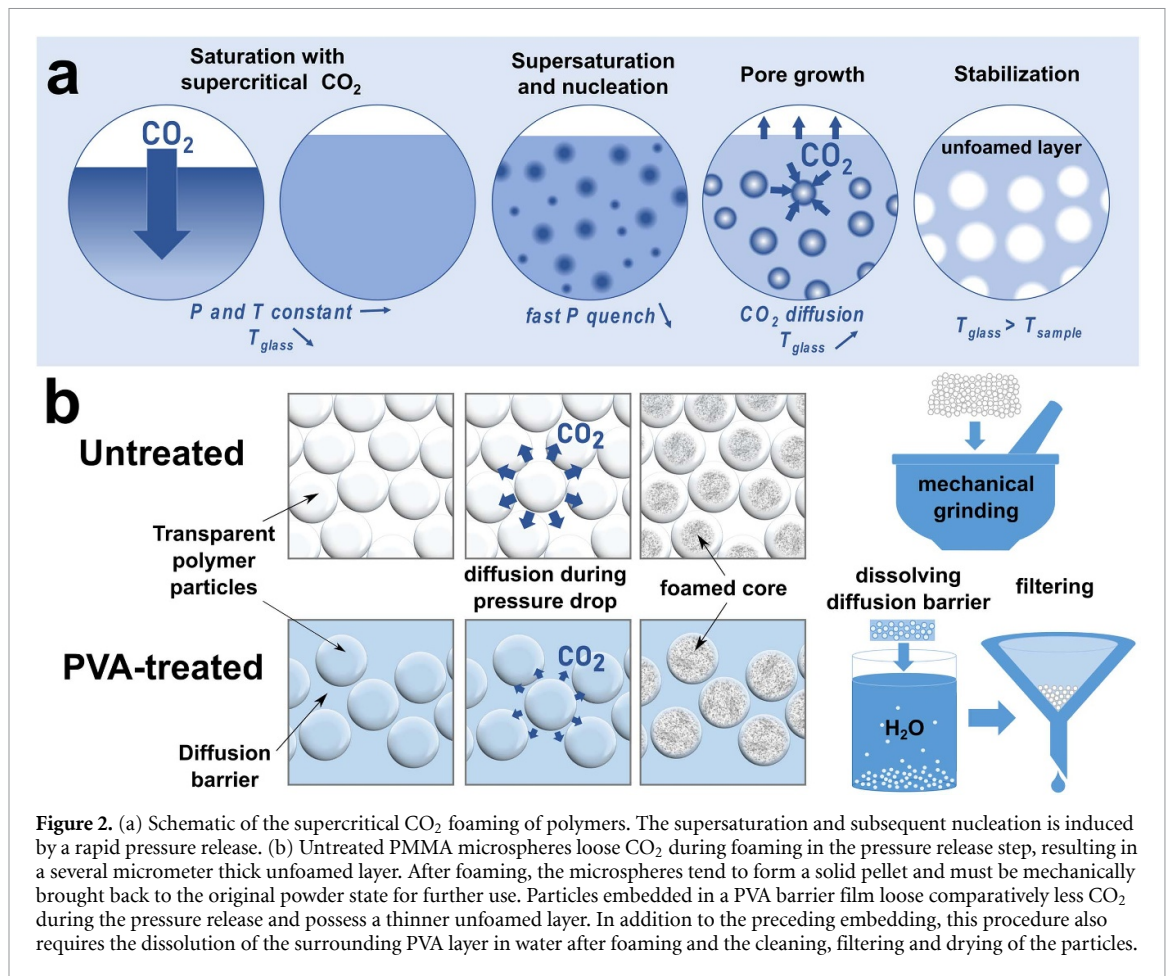
2.2. Analytical methods

2.2.1. Microscopy

For optical dark-field microscopy the microscope *Axioscope 5/7/Vario* equipped with a *Axiocam 305 color* camera and the software *ZEN core V 3.0* (all from *Carl Zeiss Microscopy GmbH*) was used. The particles were immersed in glycerol solution (*EMSURE*[®] 85% from *Sigma Aldrich* to suppress most reflections at the interface. The difference in refractive index of glycerol solution ($n = 1.45$ [46]) and PMMA ($n = 1.49$ [47]) is sufficient to perceive the outer boundaries of the particles. For scanning electron microscopy (SEM) a *Zeiss SUPRA 60 VP* was used. All samples were sputtered with silver with a nominal film thickness of 15 nm.

Phase-contrast x-ray nano-computed tomography (nano-CT) was performed in a *Carl Zeiss Xradia 810 Ultra* x-ray microscope operating with a Cr x-ray source (5.4 keV) and a fixed working distance. Each microsphere was glued atop the tip of a stainless steel pin, which was then placed on the sample holder. Imaging of the entire microspheres was carried out in large field-of-view mode (LFOV). A total of 1001 projections with a field-of-view of 64 μm² and a pixel size of 64 nm were obtained over 180 degrees, each with an exposure time of 80 s. For the assessment of the pore size and pore density, imaging was carried out over the upper central axial section of the sphere using the high-resolution mode (HRES). Thereby two imaging experiments were done with projections having a field-of-view of 16 μm² and a pixel size of 32 nm (2 × 2 binning). A total of 1001 projections were acquired, each with an exposure time of 60 s. Those two imaging experiments were virtually combined after reconstruction (see figure S1). Image reconstruction was done using the integrated software *XMReconstructor* from *Carl Zeiss AG*. A filtered back-projection algorithm was used and projections had been previously re-aligned using adaptive motion compensation to compensate for movement during the measurements. Images were exported as a stack of TIFF.

Image processing and segmentation was performed with *Avizo 9.4.0* software from *Thermo Fisher Scientific*. For LFOV measurements de-noising of the



virtual 3D images was performed using the non-local means filter in 3D using a search window of 21 voxels, a voxel comparison neighborhood of five voxels and a similarity value set to 1.0. The two HRES images from each sample were virtually aligned and stitched together using a Lanczos algorithm for the dataset merge. Image de-noising for the merged data sets was performed in two steps: first a Gaussian filter was applied in 3D with standard deviation set to 2 for all axes, then non-local means filter was applied in 3D using the same parameters as LFOV, but with a similarity value of 0.6. The segmentation of the microsphere pores in HRES was performed using the watershed algorithm, with starting seed threshold values based on entropy-criterion automatic segmentation [48, 49] applied in local regions of interest inside the sample (see figure S2). Pores with less than 15 voxels were removed to avoid noise being erroneously attributed to pores. The porosity was estimated only for the region containing pores, from six volumes of interest with $160 \times 160 \times 160$ voxels, ensuring sampling of all the regions with varying porosity within the porous core (see figure S2). The measurement in these regions was conducted in HRES mode with a voxel size of 32 nm, which is well below the size of the majority of pores inside the polymer spheres.

2.2.2. Spectroscopy

For the comparative analysis of the optical properties, foamed particles were embedded in a PMMA matrix to achieve a refractive index match. This ensures that light interactions of the porous cores will dominate, while nearly no reflections occur at the outer surface of the particles. Particles were embedded in a PMMA resin *SKresin 1390* from *S u. K Hock GmbH* with a concentration of 5 wt%. This mixture was cast in moulds and cured with UV-light *Ultra Vitalux 300W 230V E27* from *Osram*. 5–7 PMMA samples of each microsphere type to be examined were milled down and polished to a thickness of 1 mm. The spectral measurements were performed with a *Perkin Elmer Lambda 950* equipped with an integrating sphere.

2.2.3. Evaluation of thermal and mechanical stability

For evaluation of the thermal stability of the foamed particles a *HS-300 Type B Heating Stage* from *Spectro-lab* was utilized. A sample of white particles foamed in PVA at 90 °C was glued onto a 0.3 mm thick coverslip. The sample was exposed to a temperature of 60 °C–120 °C for 10 min each and the result was evaluated by optical microscopy.

Micro compression experiments on foamed and unfoamed microspheres have been conducted with a *G200* nano indenter from *Keysight Technologies*.

Particles were compressed by a diamond flat punch with 50 μm diameter. Individual particles were glued on a microscope slide and identified using the G200 optical microscope. This assured that only a single particle was compressed at a time. The stage system has a positional accuracy within 1 μm . As loading function, a constant normalized force increase of $\dot{P}/P = 0.05 \text{ s}^{-1}$ with 2 s hold segment at the peak force was chosen.

2.2.4. Paint formulation

Either foamed or unfoamed particles were added to a transparent, synthetic resin dispersion binder *GER-STAECKER Acrylbinder* at a concentration of 20 wt %. A stencil of 1 mm thickness was used to apply the paint onto a transparent PMMA substrate. The wet paint layer had a thickness of 1 mm due to the use of the stencil. After drying the layer had a thickness of about 600 μm .

3. Results and discussion

3.1. Generation of light-scattering pores

Foaming was performed at temperatures ranging from 60 °C to 150 °C at a pressure of 50 MPa with 30 min saturation time. The success of pore formation was controlled by optical dark-field microscopy as shown in figure 3. Due to light-scattering pores the foamed core can be distinguished from the unfoamed, transparent layer around it. The assessment of the unfoamed layer in the temperature range of 100 °C–140 °C showed typical average thicknesses of about 9–10.5 μm . A slight turbidity is already visible for foaming temperatures of 60 °C compared to the unfoamed microspheres. With increasing foaming temperature the scattering effect increases. Microspheres, foamed in the temperature range from 100 °C to 140 °C, have a clearly perceivable white core (see colored temperatures in figure 3). Increasing the foaming temperature further, the scattering effect reduces. The microspheres foamed at 150 °C appear as clear as the unfoamed ones. We attribute this result to the higher diffusion rates at higher temperatures [39], by which too much CO_2 diffuses out to be available for foaming. An indication for this effect is the increased thickness of the unfoamed layer of about 14 μm for the microspheres foamed at 145 °C. Consequently, the microsphere foamed at 100 °C–140 °C were selected for further evaluation of the pore size and density and corresponding changes in optical properties.

3.2. Pore sizes and density of foamed microspheres

The white appearance of some foamed particles in optical dark-field microscopy indicates scattering and thus pore sizes of approximately $\frac{\lambda}{2}$ [1]. For scattering of the visible range of light these have to be 200–400 nm in diameter. Based on this estimate it

is of interest to verify if the pores are already in a size range that allows particularly effective scattering. For spherical air pores embedded in a matrix with a refractive index of $n = 1.5$, Ross predicted the highest scattering efficiencies for an air void diameter of 225 nm [50]. This estimation is applicable at void concentrations of less than 8 % by volume [50]. Park and Hong conducted an experimental study on the light scattering of films containing hollow polymer particles of different void sizes [51]. Here a maximum scattering was achieved with particles of a void diameter of about 280 nm [51]. Auger and McLoughlin calculated the optimum void size at a void volume concentration of 15% to be around 220–250 nm depending on the theoretical framework applied [52].

Using nano-CT, we assessed the pore size and density of the foamed microspheres to determine if the pores sizes are suitable to scatter light as effectively as possible. A particular advantage of this method is that it is non-destructive and provides detailed information about the internal three-dimensional micro-structure achieved by foaming. Figure 4(a) shows the LFOV 3D virtual image from a microsphere foamed at 130 °C. It reveals the foamed core within an unfoamed layer, corresponding well with the results obtained by optical microscopy. An example of a high-resolution mode (HRES) measurement of the upper central axis of the microspheres is indicated in blue in figure 4(a). Figure 4(b) shows the corresponding 3D reconstruction with a cross-sectional view in (c). The representative cross-sectional tomographic slices (d)–(h) in figure 4 indicate the change in pore density and pore size associated with the variation of the foaming temperature. The corresponding histograms of the pore sizes (see (d)–(h) in figure 4) can be fitted with a normal or a log-normal distribution [53]. Both result in similar values, whereby in this case the normal distribution offers a better fit and is therefore used here (see supplementary material table 1). With increasing foaming temperature the average pore size increases from $181 \pm 61 \text{ nm}$ up to $295 \pm 88 \text{ nm}$ in the temperature range from 100 °C–140 °C. Thus, the average pore size corresponds well within the predicted range for efficient scattering of visible light by air voids [50–52]. The porosity initially shows a distinct increase from only $3 \pm 1 \%$ at 100 °C to $7 \pm 2 \%$ at 110 °C and finally up to $12 \pm 3 \%$ at 120 °C. Hereafter, the density remains at this value despite increasing foaming temperatures. This indicates that the maximum pore density that can be achieved under the given foaming conditions was reached. The estimated porosity for samples foamed at 100 °C–140 °C coincides very well with the range considered in previous studies [50, 52]. However, the pore morphology deviates from the assumed perfectly spherical air voids for the theoretical estimations. Volumetric images suggest that approximately

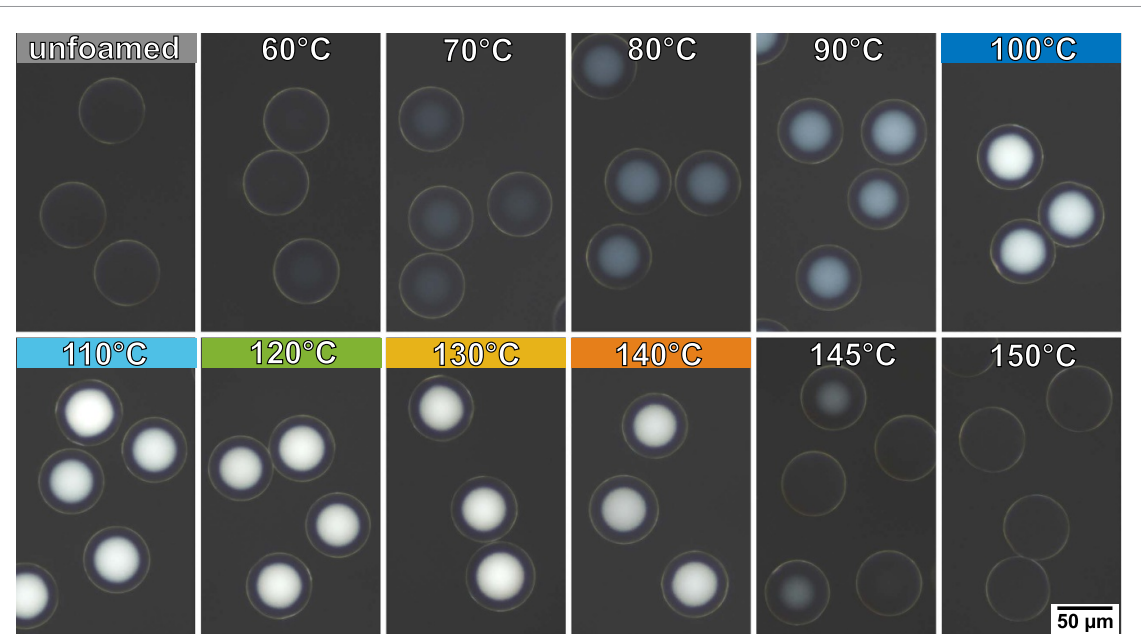


Figure 3. Optical micrographs of PMMA microspheres (nominal diameter of $60\ \mu\text{m}$) in glycerol solution, which were foamed at different temperatures with otherwise identical process parameters. The upper left image shows the microspheres before foaming. Foaming the spheres at increasing temperatures results in nanopores inside the microspheres. Here the foaming appears most efficient in a temperature range of $100\ ^\circ\text{C}$ to $140\ ^\circ\text{C}$, which is highlighted by color bars on top. With further temperature increase the foamed center becomes smaller again, until no foamed core is optically perceptible.

spherical pores merge during foaming and result in larger pores with a random shape (figures 4(b) and (c), pores in red and green color). In general, it should be noted that the above results for pore size and density are for individual exemplary microsphere samples. Thus the next step is to further investigate the optical properties of a multitude of microspheres and to determine the best parameters for foaming in terms of reflectance.

3.3. Optical properties of foamed microspheres

For comparison of the optical properties of the microspheres foamed at different parameters, these were embedded in PMMA at the same concentration. The resulting sample disks were trimmed to the same thickness. The reflectance spectra of these samples were measured over the wavelength range of $350\text{--}800\ \text{nm}$ as shown in figure 5. Plain PMMA samples as well as samples with embedded unfoamed microspheres are transparent. The reflection of only about 8% is attributed to reflections at the smooth sample surfaces. This indicates the successful refractive index matching between the PMMA microspheres and the PMMA embedding material. The low reflectance below $400\ \text{nm}$ of all samples is attributed to the short wavelength range absorption of the UV-curing PMMA resin. All foamed samples show increased reflectance with a slight decrease towards the longer wavelengths, which can be attributed to the decrease of the refractive index of PMMA from the short to the long wavelength range [47]. The nano-CT results show that the sample containing microspheres

foamed at $100\ ^\circ\text{C}$ has the smallest pore sizes of $181 \pm 61\ \text{nm}$ (see figure 4(d)). It exhibits a steep increase in reflectance towards the shorter wavelength range, while showing the lowest reflectance of all foamed samples for wavelengths of $600\text{--}800\ \text{nm}$. This can be explained by the dependence of the light scattering on the pore size, as smaller pores or particles tend to scatter short wavelengths stronger than longer wavelengths. Despite the low pore density of $3 \pm 1\%$, the reflectance is comparable to the samples foamed at $120\ ^\circ\text{C}$ – $140\ ^\circ\text{C}$, which all possess much higher pore densities (figure 4(d)). The highest reflectance is achieved for the sample foamed at $110\ ^\circ\text{C}$, although the pore density has not reached its maximum here. The corresponding pore size of $214 \pm 79\ \text{nm}$ is in good agreement with the optimal pore size of $225\ \text{nm}$ predicted by Ross [50]. With $7 \pm 2\%$ the pore density is also within the valid scope of his prediction [50, 51]. The samples foamed at $120\ ^\circ\text{C}$, $130\ ^\circ\text{C}$ and $140\ ^\circ\text{C}$ have a higher pore density all in the same range of $11\text{--}12 \pm 3\%$. Therefore the differences in reflectance between them are to be explained with the difference in pore size. The general trend of higher reflectance for shorter wavelengths could be an advantage as for many applications an increased reflection of the blue part of light is desired. This is because a bluish undertone is perceived as fresh compared to yellowish undertones [1].

3.4. Optimization towards reduced unfoamed layers

The previously achieved thickness of the unfoamed layer of around $10\ \mu\text{m}$ might be a limiting factor,

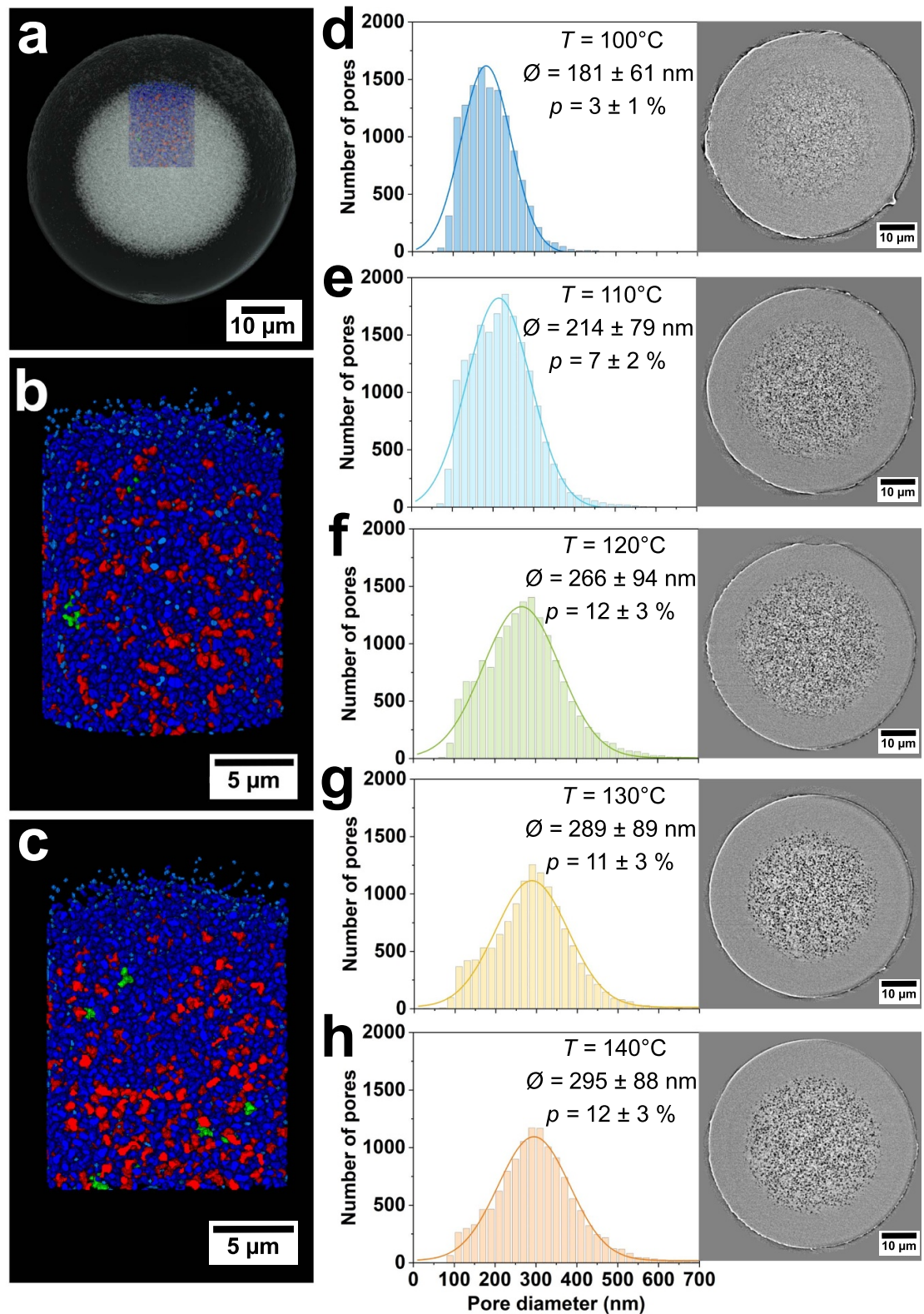
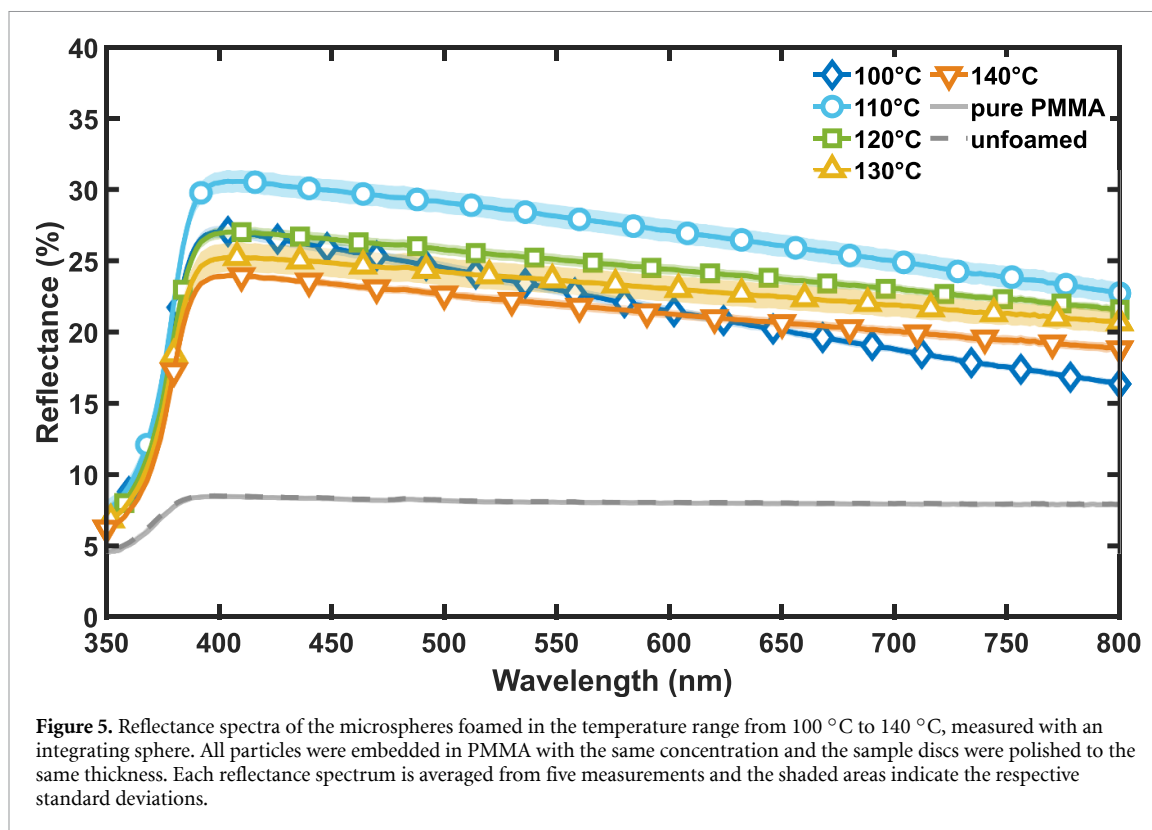


Figure 4. (a) Representative 3D virtual image of a complete foamed microsphere obtained by nano-CT. The colored slice indicates the location where high-resolution measurements were performed. (b) Virtual image of the segmented pores obtained in HRES, with the respective cross-sectional cut in (c). Colors represent pore diameters: light blue 0–250 nm, blue 250–500 nm, red 500–750 nm, green 750–1000 nm. (d)–(h) Representative cross-sectional tomographic slices of micro-spheres foamed at different temperatures with the corresponding histograms of the pore sizes, estimated average pore sizes ($\bar{\phi}$) and porosity (p).

as it reduces the number of light scattering pores in the microsphere. The reduction of this skin layer is thus addressed as an optimization target. It is

caused by the loss of CO_2 to the surroundings in the pressure release step (see figure 2(a)) [40, 54, 55]. The thickness of the unfoamed layer decreases with



increasing saturation pressure [37]. Therefore a high pressure of 50 MPa, which is the upper limit of our current setup, was applied. Orsi *et al* reported the production of hollow particles by embedding polystyrene particles (50 to 0.2 μm) in a PVA-based barrier to prevent the loss of CO_2 during the pressure release [40]. CO_2 foaming with this surrounding PVA-barrier created cavities at the particle surface, which was proposed for the use as reservoirs for encapsulation for drug delivery [40, 56, 57]. Inspired by this study we used an aqueous PVA solution as embedding solution for PMMA spheres of 60 μm diameter. After solvent evaporation the particle loaded PVA samples were foamed within the temperature range from 50 °C to 150 °C at 50 MPa, respectively. To account for the additional time needed for CO_2 to diffuse through the barrier, the saturation time was increased to 120 min [40]. After foaming the diffusion barrier was dissolved in H_2O . After filtering and drying the particles were examined with optical dark-field microscopy, as described previously. The optical microscopy images in figure 6 show the successful foaming in terms of a white color impression, which is achieved already at temperatures of 80 °C–100 °C. The unfoamed layer in this temperature range is already reduced to a thickness not resolvable by optical microscopy. Samples foamed at 110 °C or higher show a thin unfoamed layer, its formation can be attributed to an increased viscosity of the PVA barrier layer to be expected with rising temperatures. Thereby more CO_2 can escape to the surroundings. The unfoamed layer has an irregular shape due to visible deformations of the

particles. These occur mostly in the shape of rounded indentations at the surface.

The reflectance spectra measured with an integrating sphere presented in figure 7 show the reflectance of the PMMA sample discs containing particles foamed in a PVA-barrier film at 80 °C–110 °C, respectively. The sample discs have been prepared analog to the previous embedded samples (section 2.2.2). Despite the reduced unfoamed layer, the reflectance obtained is within the same range as for the microspheres foamed without a barrier film. However, the direct comparison of the samples foamed at 100 °C with and without diffusion barrier, shows an enhancement of the reflectance of a few percent over the whole spectrum (figures 5 and 7). In contrast to this, the reflectance for the PVA embedded sample foamed at 110 °C is strongly reduced compared to its pure foamed counterpart.

In summary, with otherwise equal foaming parameters the use of the PVA diffusion barrier yielded only a slight improvement of the reflectance properties. The optimal foaming temperature for high reflectance is shifted towards lower temperatures. Further investigations of the diffusion barrier concerning other molecular weights, different materials or the use of plasticizers might lead to an enhanced barrier function and thus making more CO_2 accessible to the pore formation. In general, the PVA diffusion barrier allowed the implementation of lower process temperatures, reduced unfoamed layers and has the potential to enhance the scattering properties.

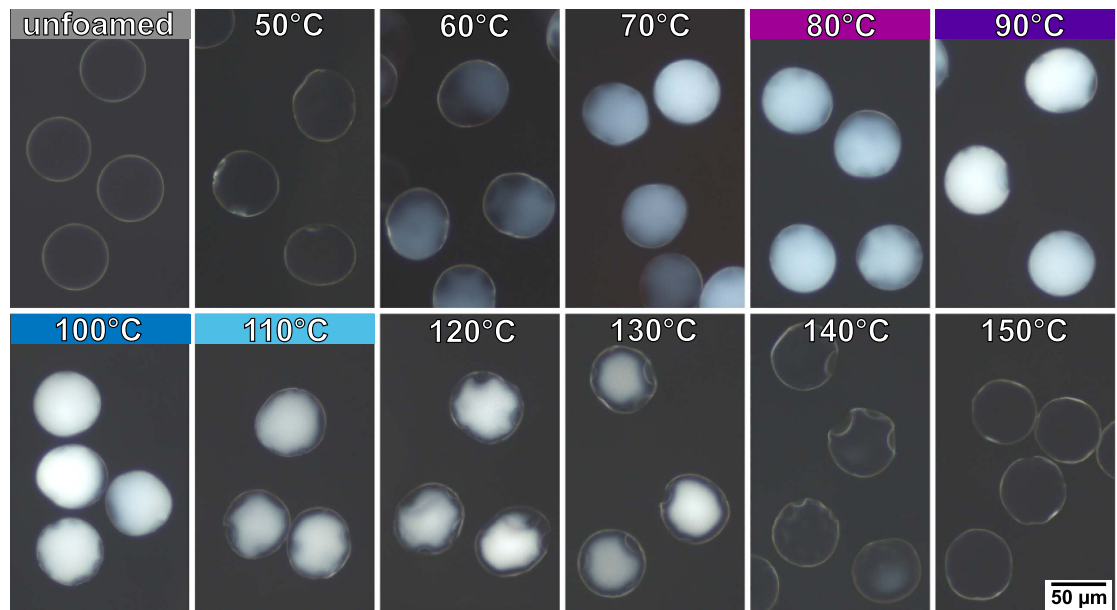


Figure 6. Micrographs of PMMA microspheres (nominal diameter of $60\ \mu\text{m}$) in glycerol solution, which were foamed at different temperatures, while being embedded within a PVA diffusion barrier layer. Here the foaming appears most efficient in a lower temperature range of $80\ ^\circ\text{C}$ – $100\ ^\circ\text{C}$, while the formation of the unfoamed skin layer is reduced and a distinct deformation of the particle shape is observable.

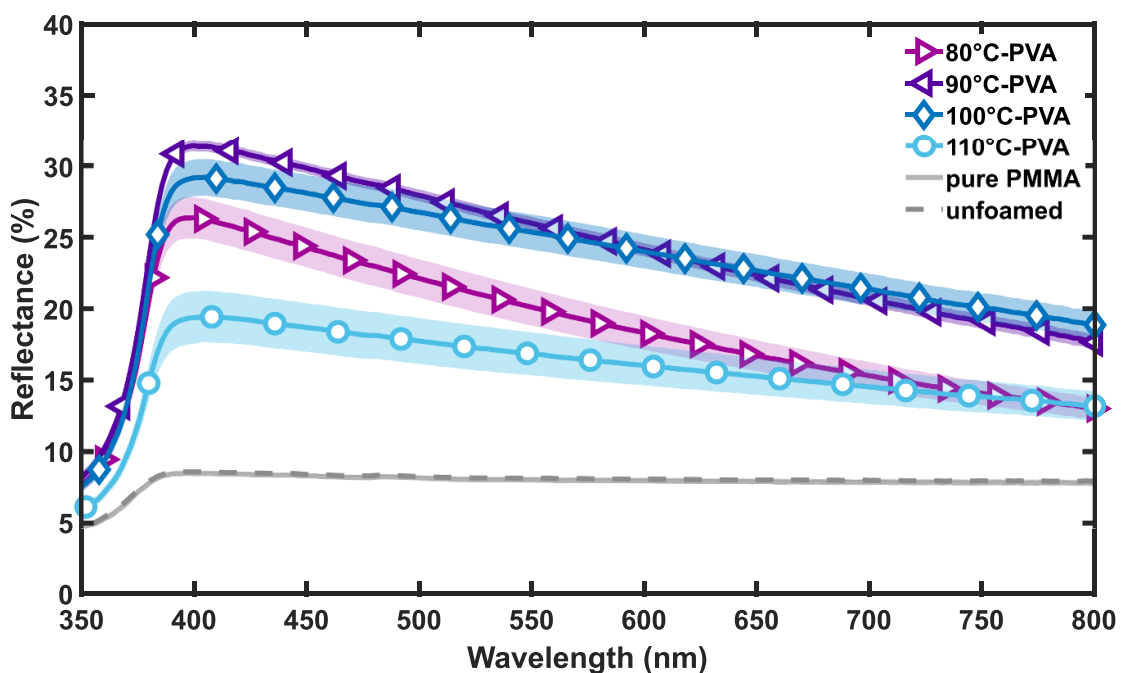


Figure 7. Reflectance spectrum of particles foamed within a PVA diffusion barrier at $80\ ^\circ\text{C}$ – $110\ ^\circ\text{C}$ measured by integrating sphere. All particles are embedded in PMMA in the same concentration and the sample discs are polished to the same thickness. The shaded areas indicate the standard deviation of 5 measurements respectively.

3.4.1. Improvement towards smaller foamed particles

For varnishes, paints and paper mostly particles smaller than $60\ \mu\text{m}$ are desired, as these products are very thin. Also, foamed particles of $60\ \mu\text{m}$ diameter are still distinguishable as granular turbidity within the embedding material, while smaller particles are not perceived as individual particles anymore. The use of a diffusion barrier could allow the foaming of smaller

particles, which otherwise loose to much CO_2 during the pressure drop to achieve a foamed core. PMMA particles of 10 , 20 and $40\ \mu\text{m}$ nominal diameter were embedded in PVA solution analog to the described procedure. Subsequently foaming was performed at temperatures of $80\ ^\circ\text{C}$, $90\ ^\circ\text{C}$ and $100\ ^\circ\text{C}$. As shown in figure 8 particles of 40 and $20\ \mu\text{m}$ diameter have a foamed core at the temperature range tested. That is a

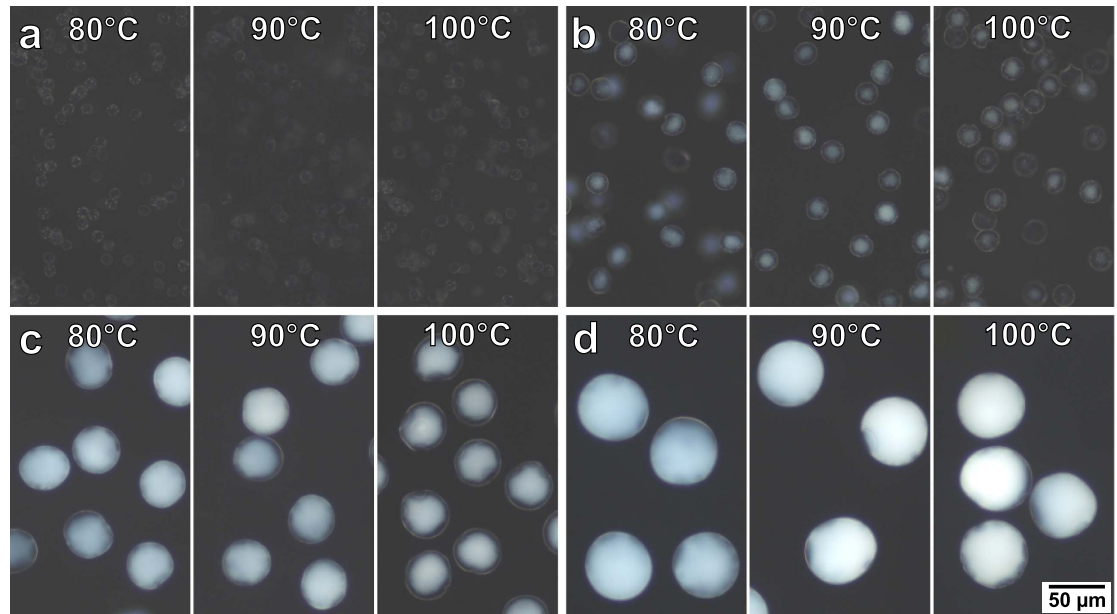


Figure 8. Foaming of PVA embedded PMMA microspheres at different temperatures increasing from 80 °C to 100 °C (left to right, respectively). The nominal diameters are (a) 10 μm , (b) 20 μm , (c) 40 μm and (d) 60 μm .

considerable improvement, as for particles of 20 μm diameter no foamed core was achieved, when foamed without diffusion barrier. Particles of 10 μm diameter do not appear to have light scattering pores and are therefore transparent. Here deformations of the samples foamed with a PVA barrier are recognizable, too. Due to the resolution limitations of optical microscopy these are further assessed by means of SEM. As evident from figure 9 the particles foamed with the diffusion barrier possess rounded pits of different sizes at their surface. We can observe here that the particles of 10 μm diameter show severe deformations (see figure 9(a) and inset). These dimples might be caused by the hindered, but nevertheless occurring, escape of gas at the particle surface. Thereby, a gas void could form in the PVA diffusion barrier, deforming the currently softened particle. For the small particles these gas voids could become large enough to create the various non-spherical particle shapes observed. In figure 9(e) we show a schematic representation of how the various observed deformations could originate from the formation of a gas void between the particle and the diffusion barrier. This explanation is supported by the SEM images of foamed particles shown in figure 9(f). These particles were preserved in their PVA embedding after foaming and show large voids in the PVA matrix in conjunction with strongly deformed particles.

The observation of rounded surface indentations is in good agreement with other studies on supercritical CO_2 foaming with a PVA-based gas diffusion barrier [40, 54, 55]. Orsi *et al* [40] described the formation of open hollows for polystyrene (PS) particles foamed in a PVA barrier film. They reported a resulting bowl shaped profile for particles with a diameter

of 5 to 0.2 μm . They observed preferential void formation close to the surface and the occasional formation of open hollows along with closed inclusions within one particle. Barroso-Solares *et al* utilized a PVA based diffusion barrier on solid polycaprolactone (PCL) fibers, thereby producing hollow fibers permeated by surface pores after pressure induced foaming [54]. Cuadra-Rodriguez *et al* successfully reduced the unfoamed layer of PMMA films with a PVA diffusion barrier and likewise reported a porous surface structure after foaming [55]. Our observations indicate a transition between the formation of nanoporous inner structures combined with surface indentations (for 60–20 μm particles), towards the sole formation of the latter without a foamed core (for 10 μm particles). As CO_2 diffuses through the surface, its concentration in the surrounding matrix is depleted [35]. Therefore it is not available for further nucleation and pore formation in close proximity [35, 37, 40]. For small particles the CO_2 concentration might be depleted by the preferential void formation close to the surface to an extent that not enough gas is left to form a foamed core [37, 40]. As the particle size decreases the surface to volume ratio becomes more and more unfavorable, which might further enhance the loss of CO_2 out of the surface. This may be hindered by the barrier film but not completely prevented.

3.5. Thermal and mechanical stability of foamed microspheres

The stability of the pore structure under heat load is important for various fields of application, as some production processes require one or more heating and drying steps. The thermal destruction of the pore

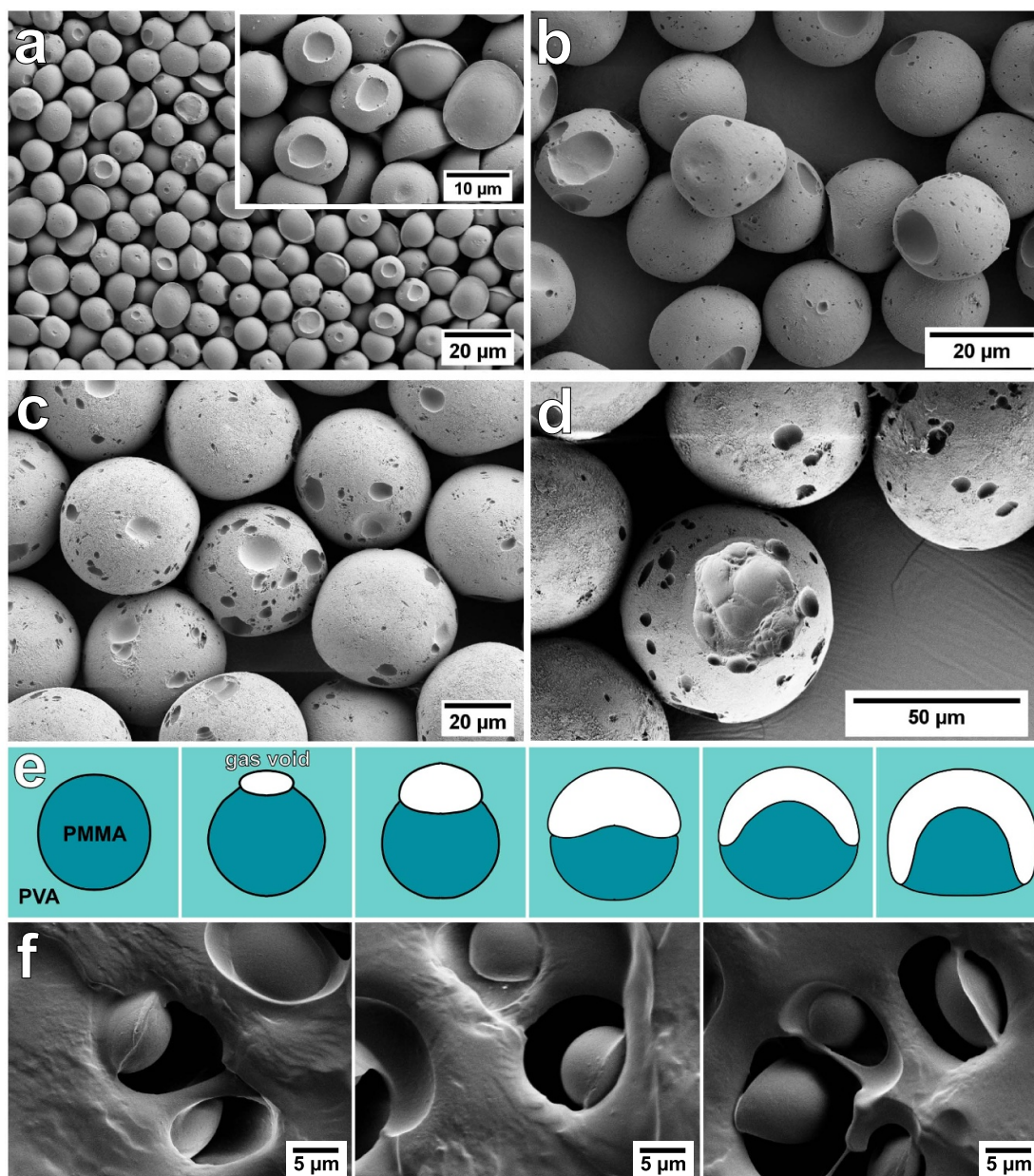


Figure 9. SEM images of PMMA particles with diameters of (a) 10 μm , (b) 20 μm , (c) 40 μm and (d) 60 μm after foaming within a PVA barrier film. All particles exhibit surface deformations. (e) A possible explanation for these deformations of the spheres is the formation of gas voids during the foaming process. Gas voids at the interface between particle and PVA barrier might be imprinted into the polymer particle, which is soft and deformable during foaming. The size and shape of the gas void thereby determines the shape of the deformation. (f) SEM images of 10 μm particles after foaming exhibit strongly pronounced deformations matching the voids formed in the surrounding barrier film.

structure and the resulting recovery of transparency was investigated using a thermostatic heating stage. When foamed 60 μm particles were heated up to 110 $^{\circ}\text{C}$ no visible change in the white color impression was observed (see figure S3). Heated further to 115 $^{\circ}\text{C}$ fading was observed and heated at 120 $^{\circ}\text{C}$ the particles turned transparent (see figure S3). This temperature-dependent loss of opacity is an important aspect to consider when processing the foamed particles.

Another aspect is the mechanical stability of the foamed particles compared to their unfoamed counterparts. Our observation has shown that the

foamed particles are mechanically stable enough to withstand manual milling in a mortar. In addition, we tested the properties of foamed and unfoamed particles using micro particle compression. A series of tests with maximum loads from 50 to 250 mN were measured in an increment of 50 mN on each type of particle. The exemplary load-displacement curve of an unfoamed and a foamed particle with the maximum load of 250 mN applied is shown in figure 10(a). Whether any fracture of the particles occurred due to the loads applied was investigated by SEM. For the unfoamed particles a clear imprint of the flat punch was observed for particles loaded with

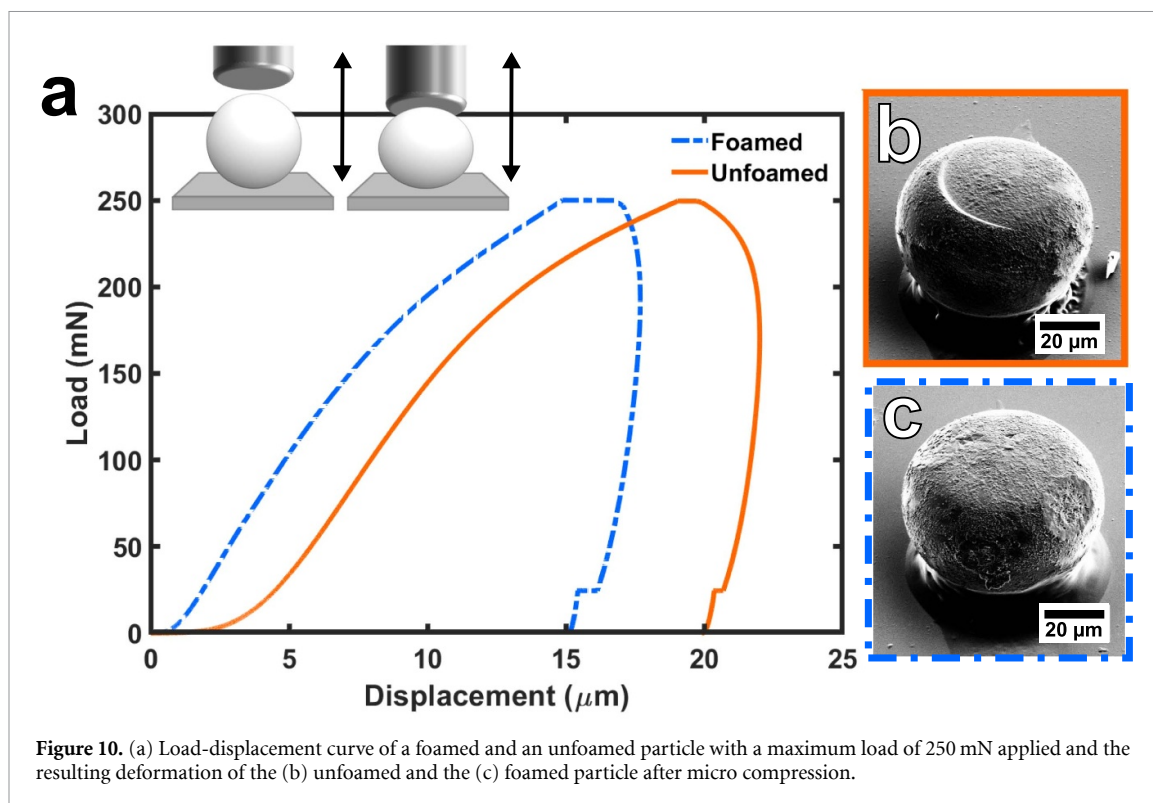


Figure 10. (a) Load-displacement curve of a foamed and an unfoamed particle with a maximum load of 250 mN applied and the resulting deformation of the (b) unfoamed and the (c) foamed particle after micro compression.

200 and 250 mN respectively, as it is shown exemplary in figure 10(b). In the case of the foamed particles, the first deformations are observed for loads of 150 mN, which get more pronounced for higher loads of 200 and 250 mN. Here, the deformation takes the form of a flattening in shape in comparison to the previous spherical particle, as shown in figure 10(c). In a multi-cycling loading-unloading experiment as shown exemplary in figure S4, hysteresis loops are found in both foamed and unfoamed particles. This demonstrates the viscoelastic behavior of both types of particles. Overall, neither was any fracture of the particles nor a loss of white color impression observed in the foamed particles due to mechanical loading.

In summary, heating at temperatures above about 115 °C causes the foamed particles to lose their white color impression. Mechanical stress can deform the overall particle shape, but the white color remains. It can therefore be assumed that the particles are well suited for applications without intense temperature loads and that the mechanical stability is not severely changed by foaming.

3.6. Practical application

The monodisperse PMMA particles used here as base material are utilized as functional additives for various paints, coatings, varnishes and lacquers to obtain super matte paints with good scratch resistance [41]. It can therefore be assumed that the particles are well suited for incorporation into various types of paints. As a proof of concept we used a transparent dispersion binder as a base for the paint formulation, used e.g. in the art sector for self-mixing of acrylic paints.

We then added either unfoamed or foamed 60 μm particles as polymeric pigments to the transparent color base. For this purpose, particles foamed at 90 °C in the process variation with PVA diffusion barrier were selected, as they reached a high reflectance in the integrating sphere measurements. The paint containing the unfoamed, transparent particles produced hardly any opaque effect as shown in figure 11(a) (left). The formulation with foamed particles resulted in a bright white color impression as shown in figure 11(a) (right). The design was created by means of a laser cutter. The particle-based paint can also be applied by brush to a classic painting base, such as a canvas, an example of which is shown in figure 11(b). Some important aspects have to be considered for an application in paint formulations. The formation of pellets and agglomerates occurs for both presented variations of foaming. Thus the foamed particles must be mechanically converted back into a lump-free powder form. Alternatively a homogenization step could be applied to the paint formulation before use. For different color formulations, differences in refractive index may occur. Therefore the required particle concentration will vary depending on the base formulation. For many paint and coating applications, the particle size is a crucial factor, as thin coatings of a few hundred micrometers or less are desired [27]. Thus typical pigments are much smaller than those presented here, which are rather in the size range of extender particles exhibiting sizes up to 50 μm [27]. However, the formation of pores in a sufficient density and size gets more challenging for smaller particle sizes. Thus the promising variation



Figure 11. (a) Comparison of a transparent base paint containing either unfoamed (left) or foamed (right) particles at a concentration of 20 wt %, shows a transparent to hazy effect for the mixture with unfoamed particles and a white, opaque coloration for mixtures with foamed particles. (b) The paint containing unfoamed (left), foamed (middle) or PVA-foamed (right) particles can be applied with a brush as well.

of foaming with a diffusion barrier should be further optimized and other suitable barrier materials should be considered.

The presented foaming process has two limiting factors. First, it is a batch process. Consequently, the foamed volume depends on the size of the autoclave. To overcome this issue, a serial process would be needed. Here, foam extrusion with supercritical CO₂ [36] followed by subsequent grinding to the desired particle size might be an option. In this case, however, the resulting particles would vary in size and lack a skin layer. Both constraints might be a drawback for some industrial application. The second limiting factor is the cumbersome addition and dissolution of the diffusion barrier. Here, it might be beneficial to coat particles in large quantities with a layer of well defined thickness. In cosmetics and pharmaceuticals powdered ingredients are often coated and numerous established manufacturing processes from laboratory to industrial scale are available [58]. Several coating techniques such as spray-drying, fluidized bed coating, or layer-by-layer coating could be applied [58] to optimize the handling of the diffusion layer.

4. Conclusion and outlook

We presented a method and favorable parameters for equipping cross-linked PMMA particles with light-scattering nanopores in a supercritical CO₂-foaming process. The successful foaming of the particles was confirmed by optical dark field microscopy. We assessed the resulting pore properties concerning pore

size and density using nano-CT. The pore sizes are in good agreement with predictions from literature for effective light scattering by air voids. Reflectance measurements of foamed particles embedded in a refractive index matching PMMA matrix demonstrated their light scattering abilities. We further optimized the foaming process by utilizing a diffusion barrier to minimize the unfoamed layer and to enable the foaming of smaller particles. The surface deformations observable after foaming with the PVA-diffusion barrier were visualized by SEM. We conclude that particles are deformed due to the formation of gas voids at the interface of particle and diffusion barrier. We further investigated how the particles react to heating and to mechanical stress through compression. The foaming does not compromise the mechanical properties of the particles, which provides important clues for their further processing. As exemplary application we presented a paint containing foamed particles. This simple color formulation created a distinct white color impression. Finally, it is worth to mention that CO₂ foaming is also applicable to bio-polymers such as polylactide [59], PCL [54] or cellulose acetate [60]. This extension to environmentally-friendly polymers opens interesting options to create renewable and bio-degradable light scattering materials for a broad range of applications.

Data availability statement

The data that support the findings of this study are available upon reasonable request from the authors.

Acknowledgments

It is a pleasure to thank our colleagues from the Institute of Microstructure Technology (IMT) and the Institute of Catalysis Research and Technology (IKFT) for their continuous support and help in the lab. We gratefully acknowledge the initiative of Julia Syurik to fabricate white polymers via foaming with supercritical CO₂ [45]. We would like to express our sincere thanks to Marcus Breig (KIT) for the photograph of the white beetle. GG would like to acknowledge funding from the Karlsruhe School of Optics & Photonics (KSOP). CSO would like to acknowledge Carl Zeiss AG for the loan of the phase-ring. This study was financially supported through the 'PROPOLIS' project funded by the Deutsche Forschungsgemeinschaft (DFG) through program DFG-SPP 1839 'Tailored disorder' (HO 2237/12-1). We acknowledge also support of the Karlsruhe Nano Micro Facility (KNMF, www.knmf.edu/knmf), a Helmholtz Research Infrastructure at Karlsruhe Institute of Technology (KIT, www.kit.edu).

ORCID iDs

Luisa Maren Borgmann  <https://orcid.org/0000-0002-6665-5830>

Juan Li  <https://orcid.org/0000-0003-2331-913X>

References

- [1] Winkler J (ed) 2013 *Titanium Dioxide: Production, Properties and Effective Usage (European Coatings Tech Files)* 2nd edn (Hanover: Vincentz Network)
- [2] Braun J H, Baidins A and Marganski R E 1992 *Prog. Org. Coat.* **20** 105–38
- [3] Gázquez M J, Bolívar J P, Garcia-Tenorio R and Vaca F 2014 *Mater. Sci. Appl.* **05** 441–58
- [4] Ruzala M J A, Rowson N A, Grover L M and Choudhery R A 2015 *Int. J. Chem. Eng. Appl.* **6** 331–40
- [5] Long T C, Saleh N, Tilton R D, Lowry G V and Veronesi B 2006 *Environ. Sci. Technol.* **40** 4346–52
- [6] Yazdi A S, Guarda G, Riteau N, Drexler S K, Tardivel A, Couillin I and Tschopp J 2010 *Proc. Natl Acad. Sci.* **107** 19449–54
- [7] Bundschuh M, Seitz F, Rosenfeldt R R and Schulz R 2012 *PLoS One* **7** e48956
- [8] Ruiz P A et al 2016 *Gut* **66** 1216–24
- [9] Proquin H, Rodríguez-Ibarra C, Moonen C G J, Ortega I M U, Briedé J J, de Kok T M, van Loveren H and Chirino Y I 2016 *Mutagenesis* **32** 139–49
- [10] Bettini S et al 2017 *Sci. Rep.* **7** 40373
- [11] Guo Z, Martucci N J, Moreno-Olivas F, Tako E and Mahler G J 2017 *NanoImpact* **5** 70–82
- [12] Pinget G et al 2019 *Front. Nutr.* **6** 57
- [13] Guillard A et al 2020 *Part. Fibre Toxicol.* **17** 51
- [14] Winkler H C, Notter T, Meyer U and Naegeli H 2018 *J. Nanobiotechnology* **16** 51
- [15] EFSA Panel on Food Additives and Flavourings (FAF) 2021 *EFSA J.* **19** 6585
- [16] Official Journal of the European Union - Document 32022R0063 2022 (available at: <http://data.europa.eu/eli/reg/2022/63/oj>)
- [17] Lee D 2007 *Nature's Palette* (Chicago, IL: University of Chicago Press)
- [18] Luke S M, Hallam B T and Vukusic P 2010 *Appl. Opt.* **49** 4246–54
- [19] Parnell A J et al 2015 *Sci. Rep.* **5** 18317
- [20] Burrelli M, Cortese L, Pattelli L, Kolle M, Vukusic P, Wiersma D S, Steiner U and Vignolini S 2014 *Sci. Rep.* **4** 6075
- [21] Vukusic P, Hallam B and Noyes J 2007 *Science* **315** 348
- [22] Cortese L, Pattelli L, Utel F, Vignolini S, Burrelli M and Wiersma D S 2015 *Adv. Opt. Mater.* **3** 1337–41
- [23] Wilts B D et al 2017 *Adv. Mater.* **30** 1702057
- [24] Leertouwer H L, Wilts B D and Stavenga D G 2011 *Opt. Express* **19** 24061
- [25] Dow Product Information: ROPAQUE™ Hollow Sphere Pigments (available at: www.dow.com/en-us/product-technology/pt-additives-modifiers/pg-additives-hollow-sphere-pigments.html) (Accessed 10 February 2023)
- [26] Dow Technical data sheet: ROPAQUE™ ULTRA E SLF Opaque Polymer (available at: www.dow.com/en-us/pdp.ropaque-ultra-e-slf-opaque-polymer.392452z.html) (Accessed 10 February 2013)
- [27] Lambourne R (ed) 1999 *Paint and Surface Coatings (Woodhead Publishing Series in Metals and Surface Engineering)* 2nd edn (Cambridge: Woodhead Publishing)
- [28] Nguyen D, Such C and Hawkett B 2011 *J. Polym. Sci. A* **50** 346–52
- [29] Zhu L, Nguyen D, Davey T, Baker M, Such C, Hawkett B S and Neto C 2017 *Polymer* **131** 10–16
- [30] Hentze H P and Antonietti M 2002 *Rev. Mol. Biotechnol.* **90** 27–53
- [31] Chiou J S, Barlow J W and Paul D R 1985 *J. Appl. Polym. Sci.* **30** 2633–42
- [32] Shieh Y T, Su J H, Manivannan G, Lee P H C, Sawan S P and Spall W D 1996 *J. Appl. Polym. Sci.* **59** 707–17
- [33] Shieh Y T, Su J H, Manivannan G, Lee P H C, Sawan S P and Spall W D 1996 *J. Appl. Polym. Sci.* **59** 695–705
- [34] Goel S K and Beckman E J 1995 *AIChE J.* **41** 357–67
- [35] Tomasko D L, Li H, Liu D, Han X, Wingert M J, Lee L J and Koelling K W 2003 *Ind. Eng. Chem. Res.* **42** 6431–56
- [36] Okolieocha C, Raps D, Subramaniam K and Altstädt V 2015 *Eur. Polym. J.* **73** 500–19
- [37] Goel S K and Beckman E J 1994 *Polym. Eng. Sci.* **34** 1148–56
- [38] Goel S K and Beckman E J 1994 *Polym. Eng. Sci.* **34** 1137–47
- [39] Nikitin L N, Said-Galiyev E E, Vinokur R A, Khokhlov A R, Gallyamov M O and Schaumburg K 2002 *Macromolecules* **35** 934–40
- [40] Orsi S, Maio E D, Iannace S and Netti P A 2014 *Nano Res.* **7** 1018–26
- [41] Microbeads (available at: <http://micro-beads.com/Applications.aspx>) (Accessed 23 April 2021)
- [42] Costeux S 2014 *J. Appl. Polym. Sci.* **131** 41239
- [43] Min K, Silberstein M and Aluru N R 2013 *J. Polym. Sci. B* **52** 444–9
- [44] Hussein M A 2017 *Int. J. Biosens. Bioelectron.* **3** 279–84
- [45] Syurik J, Siddique R H, Dollmann A, Gomard G, Schneider M, Worgull M, Wiegand G and Hölscher H 2017 *Sci. Rep.* **7** 46637
- [46] Jungermann E and Sonntag N O (eds) 1991 *Glycerine: a key Cosmetic Ingredient* vol 11 (Boca Raton, FL: CRC Press)
- [47] Sultanova N, Kasarova S and Nikolov I 2009 *Acta Phys. Pol. A* **116** 585–7
- [48] Pun T 1981 *Comput. Graph. Image Process.* **16** 210–39
- [49] Kapur J, Sahoo P and Wong A 1985 *Comput. Vis. Graph. Image Process.* **29** 273–85
- [50] Ross W D 1974 *Ind. Eng. Chem. Prod. Res. Dev.* **13** 45–49
- [51] Park J M and Hong S M 2001 *J. Ind. Eng. Chem.* **7** 23–29
- [52] Auger J C and McLoughlin D 2015 *J. Coat. Technol. Res.* **12** 693–709
- [53] Syurik J, Schwaiger R, Sudera P, Weyand S, Johnsen S, Wiegand G and Hölscher H 2017 *Beilstein J. Nanotechnol.* **8** 906–14

- [54] Barroso-Solares S, Cuadra-Rodríguez D, Rodríguez-Mendez M L, Rodríguez-Perez M A and Pinto J 2020 *J. Mater. Chem. B* **8** 8820–9
- [55] Cuadra-Rodríguez D, Barroso-Solares S, Rodríguez-Pérez M and Pinto J 2022 *Mater. Des.* **217** 110648
- [56] Contaldi V, Imperato L, Orsi S, Maio E D, Netti P A and Iannace S 2016 *J. Appl. Polym. Sci.* **133** 44236
- [57] Contaldi V, Carbone M G P, Maio E D, Manikas A C and Netti P A 2016 *RSC Adv.* **6** 64140–6
- [58] Ghosh S K (ed) 2006 *Functional Coatings* (New York: Wiley)
- [59] Frerich S C 2015 *J. Supercrit. Fluids* **96** 349–58
- [60] Reverchon E and Cardea S 2007 *J. Supercrit. Fluids* **40** 144–52